JOURNAL OF MATERIALS SCIENCE **34** (1999) 3913–3922

Mechanical properties of alkaline earth-doped lanthanum gallate

S. BASKARAN*, C. A. LEWINSOHN, Y-S. CHOU, M. QIAN, J. W. STEVENSON, T. R. ARMSTRONG
Pacific Northwest National Laboratory†, Materials and Chemical Sciences Department, P.O. Box 999, MS K2-44, Richland, WA 99352
E-mail: suresh.baskaran@pnl.gov

Lanthanum gallate doped with alkaline earths was prepared from combustion-synthesized powders. Mechanical properties of the doped gallates were evaluated as a function of composition and temperature. The indentation fracture toughness of Sr-substituted gallates was significantly better than the Ca- and Ba-substituted materials, but the toughness of all the doped gallates was significantly lower than yttria-stabilized zirconia, a typical electrolyte material. Small improvements in room temperature toughness and strength were measured in $(La_{0.9}Sr_{0.1})_xGa_{0.8}Mg_{0.2}O_{3-\delta}$, ("LSGM-1020") samples with significant A-site cation non-stoichiometry ($x = 0.9$). The flexural strength of stoichiometric LSGM-1020 decreased from ≈150 MPa at room temperature, to ≈100 MPa at higher temperatures (600–1000 °C). The notched-beam fracture toughness of LSGM-1020 decreased from ≈2.0–2.2 MPa$\sqrt{m}$ at room temperature, to ≈1.0 MPa$\sqrt{m}$ at 600 °C. The decrease in mechanical properties over this temperature range was correlated to changes in crystal structure that have been identified by neutron diffraction. These crystallographic changes were also accompanied by significant changes in the thermal expansion behavior and elastic modulus. For off-stoichiometric LSGM-1020 with A/B cation stoichiometry of 0.90, strength and toughness also decreased with temperature, but the retained toughness (≈1.5 MPa$\sqrt{m}$) at elevated temperatures was higher than the toughness of the stoichiometric LSGM material.

1. Introduction

Ceramic oxygen ion conductors are used in a number of electrochemical devices, such as solid oxide fuel cells, oxygen pumps, electrolyzers, and oxygen sensors. The electrolytes in these devices are required to exhibit high ionic conductivity, low electronic conductivity, high oxygen flux rates and adequate mechanical properties. Currently, yttria-stabilized zirconia is the electrolyte of choice, but zirconia requires an operating temperature near 1000 °C. As an alternative to zirconia, a new class of ionic conductors based on acceptor-substituted lanthanum gallate ($La_{1-x}M^{2+}_xGa_{1-y}Mg_yO_{3-\delta}$) perovskites are being investigated [1–6]. The lanthanum gallates have been reported to have higher ionic conductivity than zirconia with minimal electronic conductivity, and high stability in reduced oxygen partial pressure environments [1–6]. The gallates are particularly attractive because of the potential for lower operating temperatures (≤800 °C), which might ultimately enable the use of metal interconnects instead of the brittle, lanthanum chromite-based mixed-conductors in fuel cell devices.

The mechanical properties of the gallates are critical for long-term operation of multilayered electrical devices containing these materials. A few recent studies have reported data for some gallate compositions [7–9]. Drennan *et al.* [7] noted that the measured biaxial flexural strength of ≈55 MPa at 900 °C was much lower than the room temperature strength of ≈160 MPa for $La_{0.9}M^{2+}_{0.1}Ga_{0.8}Mg_{0.2}O_{3-\delta}$. Sammes *et al.* [8] evaluated room temperature strength and indentation fracture toughness as a function of the Mg-dopant level in $La_{0.8}Sr_{0.2}Ga_{0.8-x}Mg_xO_{3-\delta}$. We have previously reported preliminary mechanical properties for the $La_{0.9}M^{2+}_{0.1}Ga_{0.8}Mg_{0.2}O_{3-\delta}$ system [9].

It was the objective of this study to characterize the strength and toughness as a function of temperature for $La_{0.9}Sr_{0.1}Ga_{0.8}Mg_{0.2}O_{3-\delta}$, and for $(La_{0.9}Sr_{0.1})_xGa_{0.8}Mg_{0.2}O_{3-\delta}$, where x refers to the A/B cation ratio in the ABO_3 perovskite structure. The idealized perovskite structure contains an equivalent number of sites for the larger A cations and smaller B cations. In practice, some perovskite materials can be prepared containing unequal molar amounts of A and B cations (A/B cation

* Author to whom all correspondence should be addressed.
† Operated for the U.S. Dept. of Energy by Battelle Memorial Institute under contract DE-AC06-76RLO 1830.

ratio ≠1). Variations in the cationic stoichiometry (i.e., the A/B cation ratio) of other perovskite materials, including $BaTiO_3$, $LaMnO_3$, $LaCrO_3$ and lead zirconate-titanates (PZTs), are known to affect phase content, microstructure, electrical properties and/or mechanical integrity of these materials [10–15].

In the lanthanum-containing perovskites, $LaMnO_3$ and $LaCrO_3$, a slight lanthanum deficiency (A/B cation ratio <1) is preferred. Single-phase lanthanum manganite perovskites can be prepared having up to 5 mol % deficiency of La or 2 mol % deficiency of Mn. However, B-site cation deficiency (i.e., an excess of lanthanum), tends to result in the formation of La_2O_3 which hydrates readily in a humid environment [16], leading to substantial deterioration of the mechanical properties of the sintered material. Just as in $LaMnO_3$ and $LaCrO_3$, a slight lanthanum deficiency may also help to enhance the long term stability of doped $LaGaO_3$ in high temperature, humid environments.

In this study, an assessment of the strength and indentation-based mechanical properties at room temperature is presented for various lanthanum gallate compositions. In addition, the measured strength and toughness values as a function of temperature are interpreted in terms of recent observations concerning phase transitions in the gallates at temperatures below 1000 °C.

2. Experimental

Doped lanthanum gallate powders prepared by a glycine-nitrate synthesis method [17, 18] were used for fabrication of pellet samples. The base composition of pellet samples studied by indentation was: $(La_{0.9}M^{2+}_{0.1})(Ga_{0.8}Mg_{0.2})O_{3-\delta}$, with $M^{2+} = Sr^{2+}$, Ca^{2+} or Ba^{2+}. For strength and toughness studies as a function of temperature, the base composition was $(La_{0.9}Sr_{0.1})_xGa_{0.8}Mg_{0.2}O_{3-\delta}$, where x refers to the A/B cation ratio in the ABO_3 perovskite structure. In this study, the A/B cation stoichiometry (i.e., ratio of A-site cations to B-site cations), x, was varied between 0.90 and 1.00. The powders that were synthesized were calcined at temperatures ranging from 1000 to 1400 °C for 2 h in air, prior to compaction in steel dies (55 MPa). Subsequently, the pressed samples were isostatically pressed (138 MPa) and then sintered in air for 2 h at temperature (1550 °C).

The bulk densities of the sintered samples were determined by the Archimedes method using ethanol. Scanning electron microscopy (SEM) was performed on polished, thermally etched sintered specimens to characterize microstructures. Grain size was determined from linear grain intercepts [19]. The phase distributions in the synthesized and sintered materials were determined by X-ray diffraction. Sintered samples were prepared for X-ray powder diffraction analysis by grinding the samples in a mortar and pestle. The experimental diffraction patterns were collected at room temperature over a range of 15–75° 2θ (step-scanned at 0.04°/2 s) using CuK_α radiation. Semi-quantitative analysis of crystalline phase concentrations was based on comparison of observed peak heights after background subtraction. At least one peak for each phase present, typically the 100% peak, was selected for this comparison. In cases where superposition obscured the 100% peak, the strongest lowest-angle resolved peak was selected and then normalized to 100%. The sum of the heights of the selected peaks for all phases present in any given specimen was taken as the total diffracted intensity. The reported semi-quantitative phase concentrations (in wt %) were equal to the ratio of the height of the selected peak for each individual phase versus the total diffracted intensity.

Bar specimens for bend tests were fabricated from doped lanthanum gallate powders (also synthesized by a combustion synthesis technique) obtained from Praxair Specialty Ceramics (Seattle, WA). The powders were isostatically pressed into cylindrical billets at 276 MPa, ground in a mortar and pestle and then passed through a 100 mesh sieve. The sieved powder was again isostatically pressed into a billet ≈34 × 34 × 64 mm in size at 276 MPa, resulting in a green density greater than 60% of the theoretical density (ThD). The samples were sintered in air at 1550 °C for 4 h. The density of each sample was measured using the Archimedes method with ethanol, and samples with densities greater than 97% of ThD were machined into 3 × 4 × 45 mm size bars for mechanical tests. Some bars were machined with a notch midway down the span for simgle-edge notched beam fracture toughness measurements. These specimens were notched in the center of the tensile face of the specimen using a 300 μm thick diamond saw to a notch/height ratio of 0.4 (notch depth of ≈1.6 mm for the 4 mm high specimens).

The flexural strength was measured (Instron model 1125) in 1/4 four-point bending with a crosshead speed of 0.5 mm/min using a fully articulated silicon carbide fixture with a 20 mm inner span and a 40 mm outer span. The flexural strength was measured in air at 25, 200, 400, 600, 800 and 1000 °C. A minimum of five values were gathered at each temperature. Only data obtained from samples that failed from intrinsic defects at or near the surface (i.e., not corners) within the inner span were used to calculate the strength values reported. The samples were heated at approximately 20 to 25 °C/min and allowed to equilibrate for 15 min prior to testing. The fracture surfaces were analyzed by SEM.

Fracture toughness was evaluated by the indentation crack-measurement technique [20] and by the notched beam technique [21]. In the indentation technique, a 5-kg indentation load was applied by a Vickers indentor (Zwick of America, Inc., E. Windsor, CT) with a 30-s residence time. For each experimental condition, five indentations and the associated radial cracks were measured and averaged to determine the hardness and fracture toughness. The elastic moduli used in the toughness calculations were obtained on polished samples by the sonic pulse technique prior to indentation [22]. In addition, the single edge-notch beam technique was used to investigate the fracture toughness as a function of temperature. Edge-notched beams were loaded in 1/4 four-point bending with a crosshead speed of 0.5 mm/min using a fully articulated silicon carbide fixture with a 20 mm inner span and a 40 mm outer

TABLE I Room temperature mechanical properties of $La_{1-x}(M^{2+})_xGa_{1-y}Mg_yO_{3-\delta}$[a]

L(M^{2+})GM composition	Phase analysis	Relative density (% theoretical density)	Electrical conductivity $(\Omega \cdot cm)^{-1}$	Indentation K_{Ic} (MPa)	Hardness (GPa)
$La_{0.9}Sr_{0.1}Ga_{0.8}Mg_{0.2}O_{3-\delta}$ (LSGM-1020)	≈99% Perovskite ≈1% unidentified	95%	0.10	0.93 (±0.10)	7.0 (±0.3)
$La_{0.9}Ba_{0.1}Ga_{0.8}Mg_{0.2}O_{3-\delta}$ (LBGM-1020)	≈95% Perovskite ≈5% unidentified	—	0.11	0.76 (±0.07)	8.4 (±0.2)
$La_{0.9}Ca_{0.1}Ga_{0.8}Mg_{0.2}O_{3-\delta}$ (LCGM-1020)	≈93% Perovskite ≈6% unidentified ≈1% MgO	—	0.02	0.68 (±0.14)	8.6 (±0.2)
$La_{0.8}Sr_{0.2}Ga_{0.9}Mg_{0.1}O_{3-\delta}$ (LSGM-2010)	≈85% Perovskite ≈5% $SrLaGa_3O_7$ ≈10% $SrLaGaO_4$	98%	—	1.00 (±0.06)	8.2 (±0.2)
$La_{0.8}Sr_{0.2}Ga_{0.85}Mg_{0.15}O_{3-\delta}$ (LSGM-2015)	≈92% Perovskite ≈4% $SrLaGa_3O_7$ ≈3% $SrLaGaO_4$ ≈1% $La_4Ga_2O_9$	97%	0.11	1.11 (±0.10)	7.8 (±0.4)

[a]Powders were calcined at 1000 °C, pressed and sintered at 1550 °C.

TABLE II Room temperature mechanical properties of $(La_{0.9}Sr_{0.1})_xGa_{0.8}Mg_{0.2}O_{3-\delta}$[a]

A-site cation non-stoichiometry, x in $(La_{0.9}Sr_{0.1})_x(Ga_{0.8}Mg_{0.2})O_{3-\delta}$	Phase composition (by X-ray diffraction)	MgO[b] content (vol %)	Grain size (μm)	Indentation K_{Ic} (MPa$\sqrt{m}$)	Hardness (GPa)	Notched beam K_{Ic} (MPa$\sqrt{m}$)	Flexural strength (MPa)
1.00	Perovskite	<0.5%	23.5 (±2.1)	1.12 (±0.08)	7.1 (±0.3)	2.06 (±0.07)	150 (±20)
0.98	Perovskite	≈1.7%	13.6 (±1.4)	1.12 (±0.08)	7.2 (±0.3)	1.90 (±0.11)	142 (±19)
0.95	≈99% Perovskite ≈1% MgO	≈1.8%	10.7 (±0.9)	1.15 (±0.15)	7.0 (±0.3)	2.02 (±0.16)	153 (±15)
0.90	≈94% Perovskite 5% SrLaGa3O7 ≈1% MgO	≈4.6%	7.0 (±1.3)	1.19 (±0.09)	7.2 (±0.2)	2.30 (±0.10)	163 (±21)

[a]Powders were calcined at 1400 °C, pressed and sintered at 1550 °C.
[b]Obtained from SEM image analysis of polished cross sections.

span. The fracture toughness was measured in air from room temperature to 1000 °C. Five samples were tested at each temperature.

Thermal expansion measurements were carried out using a vertical pushrod dilatometer (Anter Corp., Pittsburgh, PA) with sintered samples (≈25 mm length). The samples were heated to 1200 °C at a rate of 2 °C/min in air. The thermal expansion values reported are the averages of three measurements. The elastic modulus was measured as a function of temperature by the flexural resonance method [23] on bar specimens for select compositions.

3. Results and discussion

In this paper, $(La_{0.9}Sr_{0.1})_xGa_{0.8}Mg_{0.2}O_{3-\delta}$ compositions are referred to as LSGM-1020. $(La_{0.9}Ba_{0.1})_xGa_{0.8}Mg_{0.2}O_{3-\delta}$ and $(La_{0.9}Ca_{0.1})_xGa_{0.8}Mg_{0.2}O_{3-\delta}$ compositions are referred to as LBGM-1020 and LCGM-1020, respectively. The A/B cation ratio (i.e., the ratio of total moles of A-site cations to total moles of B-site cations supplied in the synthesis of a given material) is designated by "x" in the formula.

4. Microstructure

As-synthesized, combustion-derived powders contained substantial quantities of non-perovskite phases, however, the fraction of perovskite present increased significantly upon consolidation and sintering. High density was attained with all compositions by sintering at 1550 °C, but the sintered density was influenced by powder calcination temperature. Early in this study, samples were calcined at 1000 °C, and the data reported in Table I for various compositions were obtained on samples prepared from these powders. Higher calcination temperatures (up to 1400 °C) were found to increase sintered density and phase purity, and increase the average indentation fracture toughness: from 0.93 MPa$\sqrt{m}$ for samples prepared with powders calcined at 1000 °C, to 1.12 MPa$\sqrt{m}$ for samples prepared with powders calcined at 1400 °C. Later indentation characterization, including evaluation of compositions with A-site cation non-stoichiometry (Table II) was performed on samples prepared from powders calcined at 1400 °C.

Sintered LSGM-1020 with $x = 0.98$ and $x = 1.00$ were single phase perovskites (within the limitations of the XRD technique). Compositions with substantial A-site cation deficiency ($x = 0.95$, $x = 0.90$) contained significant quantities of Ga- or Mg-rich phases ($SrLaGa_3O_7$, MgO). Average grain sizes of LSGM-1020 sintered at 1550 °C are reported as a function of A/B cation ratio in Table II. The largest average

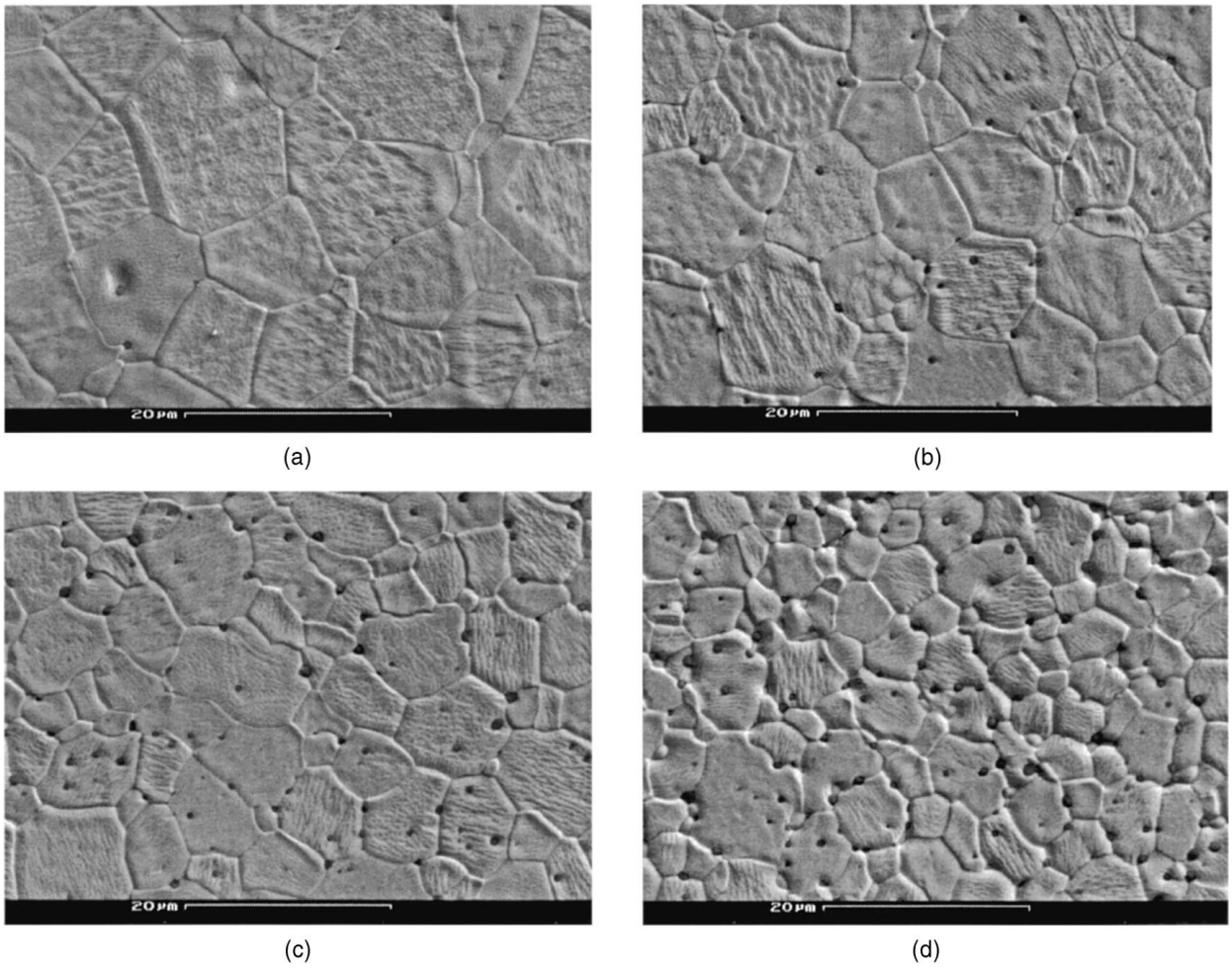

Figure 1 SEM micrographs showing microstructure of LSGM-1020 materials with two different A/B cation stoichiometry: (a) A/B = 1.00; (b) A/B = 0.98; (c) A/B = 0.95; and (d) A/B = 0.90.

grain size occurred in compositions with a stoichiometric A/B cation ratio; the average grain size decreased substantially from ≈23.5 to ≈7.0 μm as the A/B ratio was decreased from 1.00 to 0.90. SEM micrographs for LSGM-1020 with $x = 1.00$, 0.98, 0.95 and 0.90 (sintered at 1550 °C) are shown in Fig. 1a–d. The small dark inclusions in the microstructures were determined to be MgO using energy dispersive spectrometry. Since the amount of second phases in LSGM-1020 increased as the A/B ratio decreased, the observed reduction in average grain size with decreasing A/B ratio was most likely due to a reduction in grain boundary mobility caused by the presence of the second phase inclusions at the grain boundaries [24, 25]. Spherical particles of MgO are visible both within the grains and at the grain boundaries in LSGM-1020 with $x = 0.90$ (Fig. 1d); a trace amount of MgO (too small to be revealed by the XRD analysis) was also evident in the microstructure of LSGM-1020 with $x = 1.00$ (Fig. 1a).

5. Room temperature mechanical properties

The room temperature indentation fracture toughness is compared in Table I for several LSGM compositions and lanthanum gallate compositions doped with Ca and Ba. The fracture toughness obtained by the indentation method is typically less than toughness measured by other macroscopic techniques such as the notched beam method [26], but it is useful for comparison between various compositions. The indentation toughness of polycrystalline LSGM compositions is in the range of 0.9–1.1 MPa$\sqrt{}$m, while the hardness is 7.0–8.2 GPa. The reported indentation toughness and hardness of single crystal lanthanum gallate ($LaGaO_3$) are 0.7 MPa$\sqrt{}$m and 9.4 GPa, respectively [27]. The toughness for the polycrystalline LSGM-1020 is significantly higher than single-crystal $LaGaO_3$ but the lower hardness of the polycrystalline LSGM compared to the single crystal is simply indicative of the decreased resistance to penetration of a polycrystalline assemblage.

The early work by Ishihara *et al.* [1] and the work of Petric *et al.* [28] had indicated that the Sr-substituted lanthanum gallates were significantly more conductive than Ca- and Ba-substituted materials. However, the recent work by Stevenson *et al.* [9] with combustion-synthesized materials indicates that conductivity of L(Ba)GM-1020 and LSGM-1020 are almost identical, but the L(Ca)GM-1020 exhibits lower conductivity. Conductivity values at 800 °C from the work of Stevenson *et al.* [9] and the indentation toughness are compared in Table I. The indentation toughness of the Ba- and Ca- substituted gallates are significantly lower (by >20%) than the toughness of LSGM-1020, which suggests that substitution of Sr by other alkaline earths

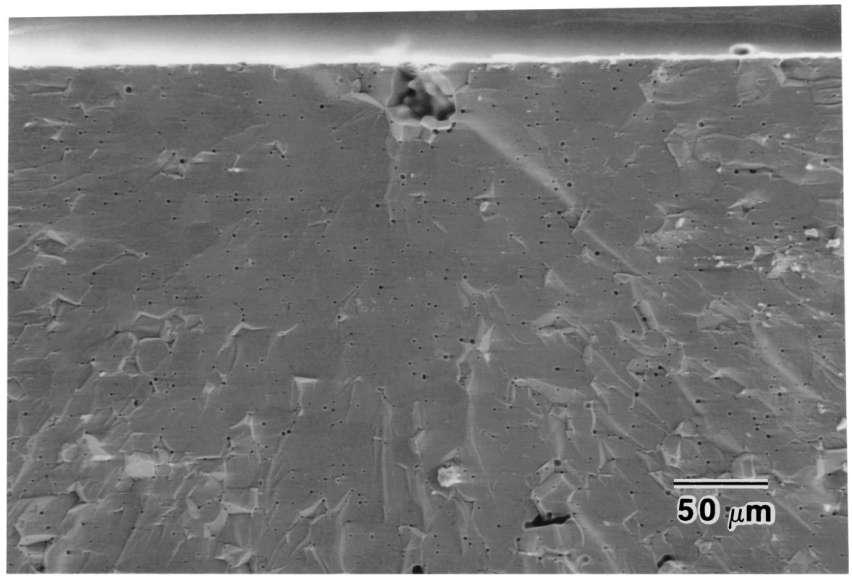

Figure 2 SEM micrograph showing fracture surface and fracture origin for stoichiometric LSGM-1020 tested at room temperature.

does not offer any advantage at least in terms of mechanical integrity. The lower toughness may be a result of lower density, but estimation of the relative density was not possible because the Ba- and Ca-substituted materials contained >5% of non-perovskite second phases. The indentation fracture toughness of all the lanthanum gallates were significantly lower than the corresponding value (2–3 MPa$\sqrt{}$m) for polycrystalline cubic zirconia electrolyte materials [29].

The flexural strength values of the LSGM-1020 compositions at room temperature for various A/B cation non-stoichiometry are listed in Table II. For A/B = 0.95–1.00, the measured strengths at room temperature were ≈150 ± 25 MPa; these values are similar to results reported in recent work by Drennan *et al.* [7] on LSGM-1020 with $x = 1.00$, where the average room temperature strength was ≈162 ± 14 MPa. The strength of LSGM is comparable to the strength of alkaline earth doped lanthanum chromites [30], but is lower than the strength (≈250 MPa) of cubic yttria-stabilized zirconia [31, 32].

The strength of LSGM-1020 for an A/B ratio of 0.90 was slightly (≈10%) higher than the strength corresponding to the compositions with other A/B cation ratios, $x = 0.95$–1.00. Similarly, the fracture toughness, both by the indentation and notched beam technique was also slightly higher for the composition with $x = 0.90$ compared to the LSGMs with higher A/B cation ratios, $x = 0.95$–1.00. If significant, the higher strength and toughness for the $x = 0.90$ material may be related to the smaller grain size, as was observed in polished sections (Fig. 1a–d and Table II). Fracture surfaces of samples tested at room temperature also indicate that similar decreases in average grain size occurred with increasing A/B cation non-stoichiometry in the samples prepared from commercial powders. However, the increase in strength and toughness could not be unequivocally correlated to a grain size effect. SEM inspection of fracture surfaces showed that the fracture was predominantly transgranular, and fracture origins were larger than the grain size. The relatively featureless fracture surface and fracture origin of a typical LSGM-1020 material with $x = 1.00$ at room temperature is shown in Fig. 2.

The higher toughness of the off-stoichiometric LSGM with A/B cation ratio of 0.90 may also be a consequence of the significant amounts of second phases, especially MgO, which was present as both intragranular and intergranular inclusions. The physical and mechanical properties of $SrLaGa_3O_7$ are not widely reported, however, the properties of MgO are well known [27, 33]. The elastic modulus of MgO is ≈300 GPa at room temperature and the thermal expansion coefficient of MgO (12–$17 \times 10^{-6}\,^{\circ}C^{-1}$ from 200–2000 °C) is also higher than that of LSGM. The toughness of single-crystal MgO (≈1.3 MPa$\sqrt{}$m) is significantly higher than that of single-crystal $LaGaO_3$ (≈0.7 MPa$\sqrt{}$m). Due to the modulus and thermal expansion mismatch, the MgO particles, although present only as a small volume fraction (≤5 vol %), can serve to deflect cracks and result in a modest enhancement in fracture toughness [34, 35]. An example of crack deflection around a MgO inclusion in LSGM-1020 with $x = 0.90$ is shown in the TEM micrograph in Fig. 3.

6. Temperature dependence of mechanical properties

6.1. Thermal expansion

Linear thermal expansion coefficients (TEC) for LSGM-1020, $x = 1.00$ and 0.90 were measured on sintered specimens over the temperature range 25 to 1200 °C. The linear expansion behavior as a function of temperature is shown in Fig. 4. (The expansion data for the sample with A-site non-stoichiometry ($x = 0.90$) is shown offset to the right by 40 °C for clarity.) Unlike the undoped $LaGaO_3$ [25], no sharp discontinuities in the dilatometer trace were evident across the temperature range, for either composition. However, both materials show a distinct change in slope around 550–600 °C, with a low thermal expansion coefficient ($\approx 10 \times 10^{-6}\,^{\circ}C^{-1}$) at the lower temperature

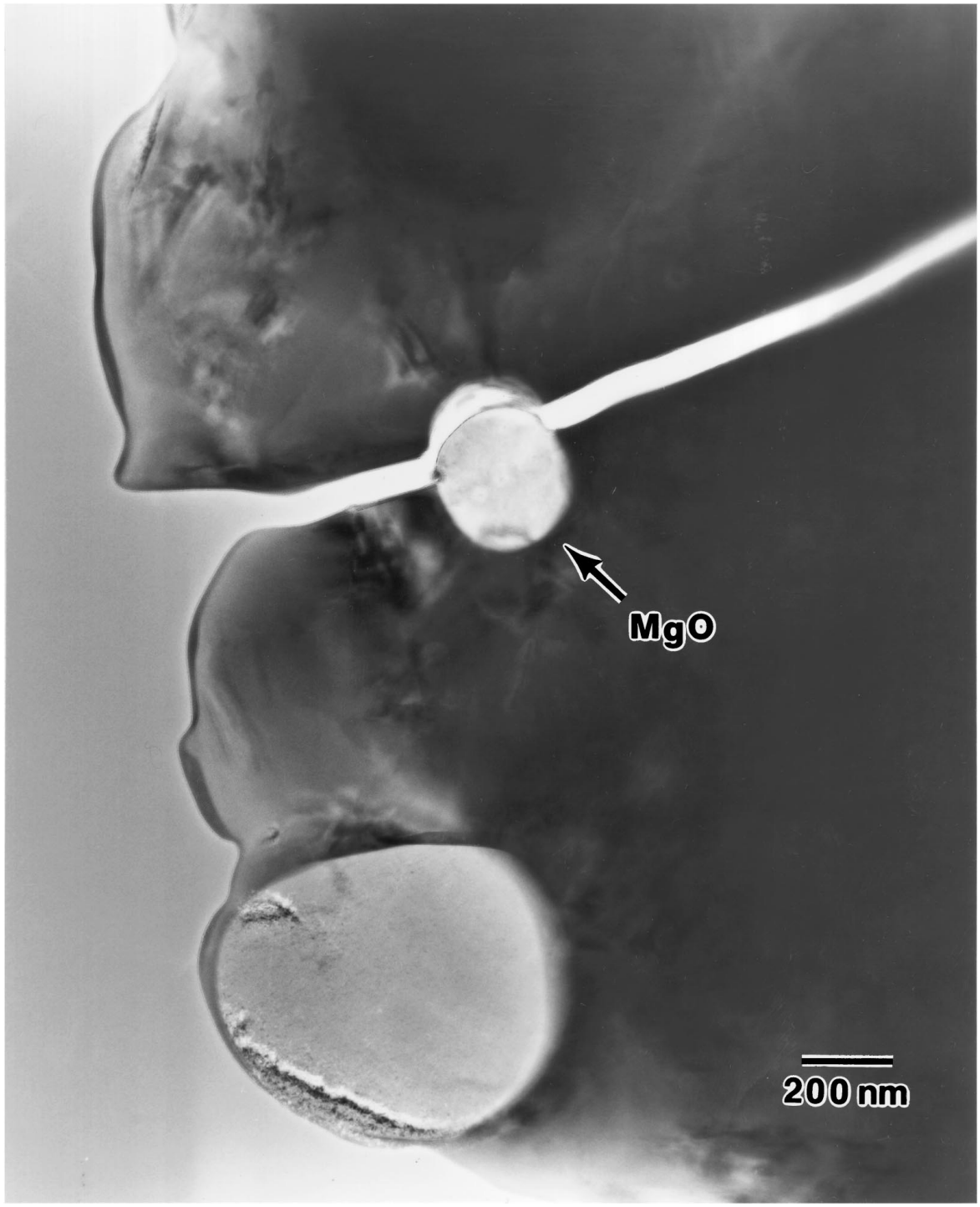

Figure 3 TEM bright field image showing microstructure of LSGM-1020, $x = 0.90$, and crack propagation around a MgO inclusion.

range, and a much higher expansion coefficient (13.5–$14.0 \times 10^{-6}\,^{\circ}C^{-1}$) above 600 °C. A similar increase in expansion coefficient for an LSGM-1020 material from $\approx$9.7–$10.5 \times 10^{-6}\,^{\circ}C^{-1}$ below 500 °C to 10.5–$11.5 \times 10^{-6}\,^{\circ}C^{-1}$ over 600 °C was noted by Tietz [36]. Tietz also observed a discontinuity in the expansion behavior, with the expansion coefficient decreasing slightly around 530 °C before increasing again with temperature. The expansion behavior for these materials correlates closely with the transition in this temperature range from monoclinic phase types to the rhombohedral phase and the associated structural changes in the lattice that has been recently characterized by neutron diffraction [37]. From the diffraction information, Slater *et al.* [37] have also calculated a distinct increase in the slope of the lattice cell volume per formula unit as a function of temperature around 500 °C, which accompanies this phase transformation.

6.2. Flexural strength

These phase transformations at 300–600 °C and the resulting changes in expansion behavior are also accompanied by a significant decrease in strength, elastic modulus, and toughness with increasing temperature. Four point bend strength as a function of test temperature for LSGM-1020, $x = 1.00$ and 0.90, is shown in Fig. 5. The measured strength of LSGM-1020

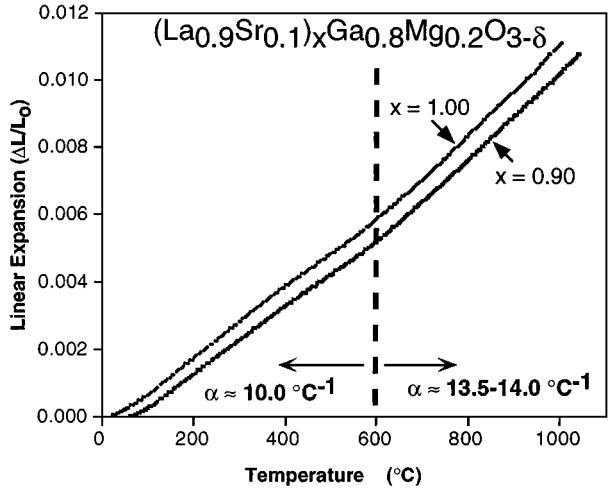

Figure 4 Linear expansion as a function of temperature for LSGM-1020 with A/B cation stoichiometry of 1.00 and 0.90.

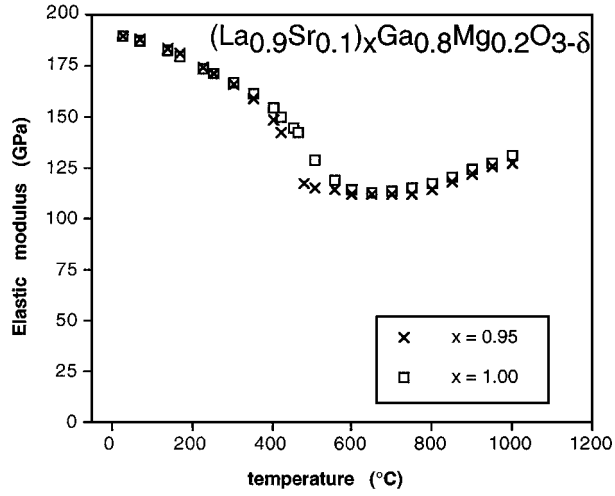

Figure 6 Elastic modulus measured by the resonance method as a function of temperature for LSGM-1020 with A/B cation stoichiometry of 1.00 and 0.95.

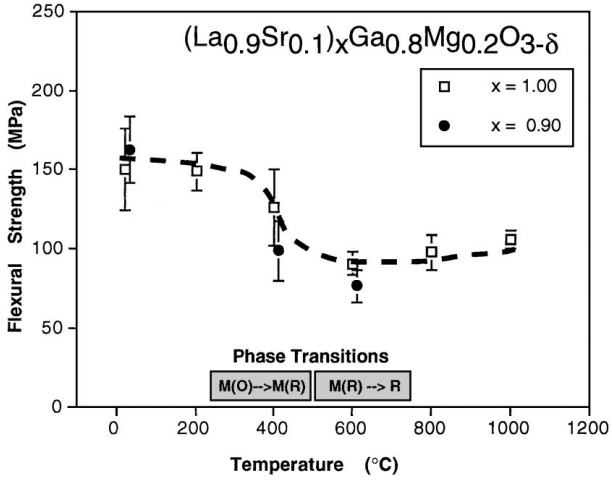

Figure 5 Flexural strength as a function of temperature for LSGM-1020 with A/B cation stoichiometry of 1.00 and 0.90. Temperature ranges observed for the phase transformations by high temperature neutron diffraction (Ref. [35]) are also shown.

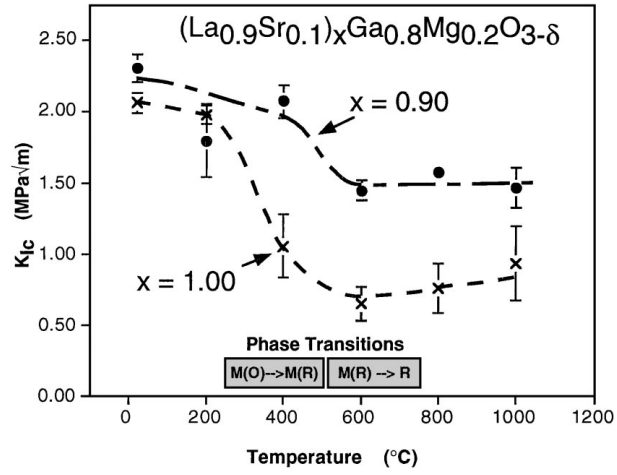

Figure 7 Fracture toughness as a function of temperature for LSGM-1020 with A/B cation stoichiometry of 1.00 and 0.90.

with $x = 1.00$ was lower at elevated temperatures than at room temperature; over the range 600 to 1000 °C, the strength was essentially constant at 100 ± 10 MPa. In comparison, Drennan *et al.* [7] reported very low strength at 900 °C measured in biaxial flexure: for LSGM-1020 with $x = 1.00$ at 900 °C, the measured average strength in the work of Drennan *et al.* [7] was only $\approx 55 \pm 11$ MPa.

6.3. Elastic modulus

The elastic modulus measured by the flexural resonance method ( ) is shown as a function of temperature in Fig. 6. The elastic modulus decreases steadily with temperature for LSGM-1020 with $x = 1.00$ and 0.95, with the rate of decrease in modulus being highest around 500 °C. The significant change in the modulus in this temperature range appears to closely correlate with the structural changes in the lattice and changes in the thermal expansion behavior.

6.4. Fracture toughness and fracture behavior

Fracture toughness, measured by the notched beam technique, as a function of temperature is shown in Fig. 7. The notched beam toughness of stoichiometric ($x = 1.00$) LSGM-1020 was 2.0 to 2.2 MPa$\sqrt{\text{m}}$ at room temperature, but decreased significantly to ≤ 1.0 MPa$\sqrt{\text{m}}$ at 600–1000 °C. In comparison, the fracture toughness of LSGM-1020 with $x = 0.90$ decreased with temperature in the range 400–600 °C, but this decrease was not as great (from ≈ 2.3 to ≈ 1.5 MPa$\sqrt{\text{m}}$).

For linear elastic brittle materials, changes in the fracture toughness with temperature is expected to scale with $(E\gamma)^{0.5}$, where E is the modulus and γ is the effective fracture surface energy. Both the fracture toughness and elastic modulus decrease significantly over a narrow temperature range, but the net loss in toughness is also indicative of microstructural effects on the fracture process. The stoichiometric LSGM-1020 ($x = 1.00$) showed predominantly transgranular fracture at all temperatures, and a significant decrease in fracture toughness with increasing temperature. An example of a fracture origin and the transgranular fracture

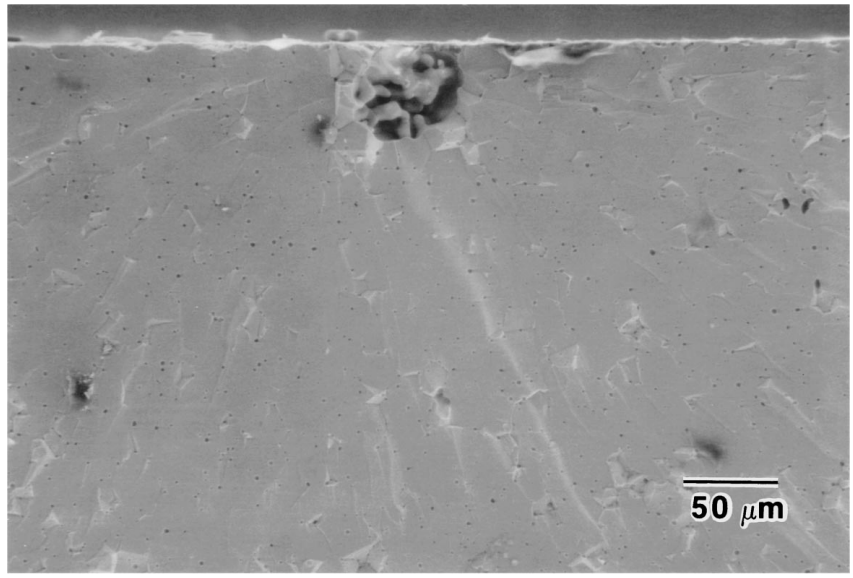

Figure 8 SEM micrograph showing fracture surface and fracture origin for stoichiometric LSGM-1020 tested at 600 °C.

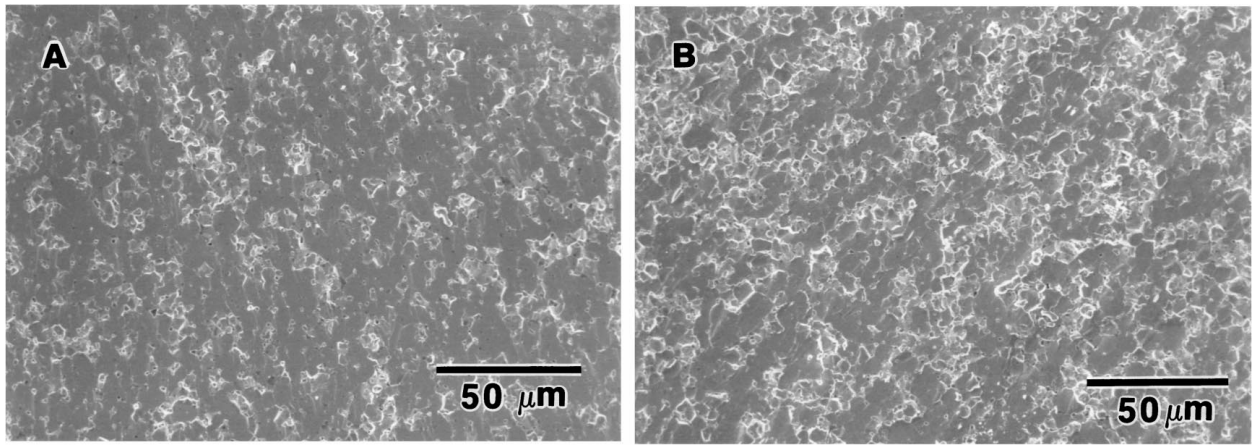

Figure 9 SEM micrograph showing fracture surfaces of off-stoichiometric (A/B = 0.90) LSGM-1020 tested at (A) room temperature and (B) 1000 °C.

morphology for LSGM-1020 ($x = 1.00$) at a test temperature of 600 °C is shown in Fig. 8. The flaw sizes in bend specimens of LSGM-1020 with the stoichiometric composition ($x = 1.00$) were 20–50 μm (e.g. fracture origins in Figs 2 and 8).

The higher fracture toughness for the off-stoichiometric ($x = 0.90$) composition at the elevated temperatures may be due to the finer grain structure and/or the presence of second phase inclusions, specifically MgO and $LaSrGa_3O_7$, observed in the microstructure, either of which could change the fracture morphology. At elevated temperatures, the fracture morphology for the off-stoichiometric material appears to be different from the fracture morphology at room temperature. Fracture surfaces of specimens with $x = 0.90$ that were tested at room temperature and at 1000 °C are shown in Fig. 9A and B, respectively. Fracture morphology appears to change with temperature in the sample with significant A-site cation non-stoichiometry, with the grain boundaries being more highly accentuated in the specimen fractured at 1000 °C (Fig. 9B). Such accentuation of the grain structure is not likely to be a result of thermal etching since the test temperature was at least 500 °C lower than the sintering temperature, and the residence time after fracture was only a few seconds before the test furnace was switched off. As noted earlier in the discussion of the room-temperature properties, the presence of second phase inclusions such as MgO can serve to increase toughness by causing more tortuous crack propagation. Changes in the internal stresses due to the phase transformations (at $\geq$500 °C) could also potentially enhance the effect of the second phases, since differences in the physical/mechanical properties (e.g., modulus) between the LSGM phase (see Fig. 6) and MgO are magnified at the higher temperatures, which can result in increased toughness relative to the stoichiometric material.

The higher overall toughness for the $x = 0.90$ at the elevated temperatures ($\geq$600 °C) however did not translate to higher retained strength (see Figs 5 and 7). This strength/toughness observation may be related to relative sizes of fracture origins in these materials. From SEM fractography, fracture origins in the fractured surfaces of the off-stoichiometric specimens were clearly defined only in a few of the samples after testing at 600 °C, but the flaws in these samples were found to be

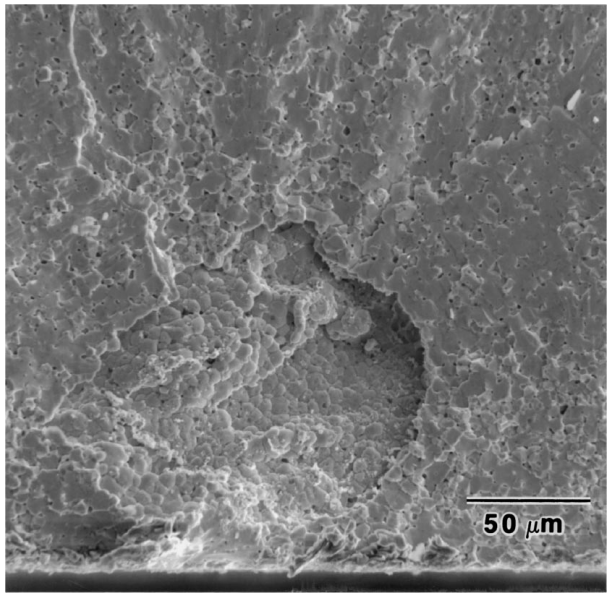

Figure 10 SEM micrograph showing fracture surface and failure origin for off-stoichiometric (A/B =0.90) LSGM-1020 tested at 600 °C.

significantly larger in size (flaw sizes of ≈80–150 μm) than the flaws in the stoichiometric material (flaw sizes of ≈20–50 μm). An example of such a large fracture origin in a bend specimen with the $x = 0.90$ composition that was tested at 600 °C is shown in Fig. 10. The reasons for larger fracture origins at high temperatures in the $x = 0.90$ composition are not clear. At low temperatures, the flaw sizes corresponding to the $x = 0.9$ composition were similar to $x = 1.0$ in the range of 20–50 μm. Although billets corresponding to each compositions were all fabricated in the same manner, both in terms of powder synthesis and forming, it is possible there are differences in the green microstructure (e.g., different agglomerate sizes) that lead to different flaw sizes after sintering. However, it is also possible that larger fracture origins at the higher temperature in the off-stoichiometric ($x = 0.90$) material containing second phases are a result of sub-critical crack growth prior to failure and this needs further investigation.

The principal conclusion from the fracture behavior and the modulus measurements at elevated temperatures for the LSGM materials is that the distinct loss in mechanical properties over a narrow low-temperature range is a result of the phase transformations and the associated structural changes, and this may affect the performance of these material at the intended operating temperature (≤800 °C), especially if components/devices undergo thermal cycles across this range. The effect of temperature cycling on mechanical integrity, particularly in different environments, deserves further study. A preliminary experiment showed that bar specimens of the stoichiometric LSGM-1020 that had been annealed at 800 °C for 5 h in air actually showed improved room-temperature strength, 188 ± 18 MPa compared to a strength of 150 ± 25 MPa for the unannealed material. The strength and toughness measurements in this study also suggest that the off-stoichiometric material ($x = 0.90$ in LSGM-1020) with slightly improved damage tolerance, i.e. fracture toughness at the operating temperatures, may offer some marginal benefits over the stoichiometric composition in device applications.

7. Conclusions

The indentation fracture toughness of all the doped gallates was significantly lower than typical zirconia electrolyte materials, but the mechanical integrity of Sr-substituted gallates was significantly better than the Ca- and Ba-substituted materials. Small improvements in room temperature toughness and strength were noted in LSGM samples with significant A-site cation non-stoichiometry. The flexural strength of stoichiometric LSGM-1020 was measured to be ≈150 MPa at room temperature, but the strength decreased to ≈100 MPa at higher temperatures (600–1000 °C). The fracture toughness of LSGM-1020 measured by notched beam measurements was ≈2.0–2.2 MPa$\sqrt{\text{m}}$ at room temperature, decreasing to ≈1.0 MPa$\sqrt{\text{m}}$ over a temperature range of 400–600 °C. The decrease in mechanical properties over this temperature range is a consequence of changes in crystal structure that have been identified by neutron diffraction. These crystallographic changes are also accompanied by significant changes in the expansion behavior and elastic modulus.

For off-stoichiometric LSGM-1020 with A/B cation stoichiometry of 0.90, the fracture toughness also decreased with temperature, but the retained toughness (≈1.5 MPa$\sqrt{\text{m}}$) at elevated temperatures was higher than the toughness of the stoichiometric LSGM material. The microstructure of the off-stoichiometric LSGM composition contained significant quantities of non-perovskite phases, MgO and $LaSrGa_3O_7$, both within the grains and at the grain boundaries, which altered the fracture behavior relative to the stoichiometric (A/B = 1.00) composition.

References

1. T. ISHIHARA, H. MATSUDA and Y. TAKITA, *J. Amer. Chem. Soc.* **116** (1994) 3801.
2. M. FENG and J. B. GOODENOUGH, *J. Solid State Inorg. Chem.* **31** (1994) 663.
3. T. ISHIHARA, H. MATSUDA and Y. TAKITA, *Solid State Ionics* **79** (1995) 147.
4. T. ISHIHARA, Y. HIEI and Y. TAKITA, *ibid.* **79** (1995) 371.
5. T. ISHIHARA, H. MINAMI, H. MATSUDA and Y. TIKATA, "Solid Oxide Fuel Cells V," edited by U. Stimming, S. C. Singhal, H. Tagawa and W. Lehnert, PV 97-40 (Electrochemical Soc., Pennington, NJ, 1997).
6. K. HUANG, M. FENG and J. B. GOODENOUGH, *J. Amer. Cer. Soc.* **79** (1996) 1100.
7. J. DRENNAN, V. ZELIZKO, D. HAY, F. T. CIACCHI, S. RAJENDRAN and S. P. S. BADWAL, *J. Mater. Chem.* **7**(1) (1997) 79–83.
8. N. M. SAMMES, M. KEPPELER, H. NAFE, F. ALDINGER and G. A. TOMPSETT, in "Proceedings of the Third European Solid Oxide Fuel Cell Forum" (European Fuel Cell Forum, Oberrohrdorf, Switzerland 1998) pp. 397–406.
9. J. W. STEVENSON, L. R. PEDERSON, J. LI, C. A. LEWINSOHN, S. BASKARAN and T. R. ARMSTRONG, *Solid State Ionics* (1998), **113–115** (1998) 571.
10. A. K. MAURICE and R. C. BUCHANAN, *Ferroelectrics* **74** (1982) 61.
11. B. JAFFE, W. R. COOK and H. JAFFE, "Piezoelectric Ceramics" (Academic Press, New York, 1971).

12. R. C. POHANKA, S. W. FREIMAN, K. OKAZAKI and S. TASHIRO, in "Fracture Mechanics of Ceramics," Vol. 5, edited by R. C. Bradt, A. G. Evans, D. P. H. Hasselman and F. F. Lange (Plenum Press, New York, NY) pp. 353–364.
13. J. W. STEVENSON, P. F. HALLMAN, T. R. ARMSTRONG and L. A. CHICK, *J. Amer. Cer. Soc.* **78** (1995) 507.
14. S. OTOSHI, H. SASKAI, H. OHNISHI, M. HSAE, K. ISHIMARU, M. IPPOMMATSU, T. HIGUCHI, M. MIYAYAMA and H. YANAGIDA, *J. Electrochem. Soc.* **138** (1991) 1519.
15. L. A. CHICK, J. LIU, J. W. STEVENSON, T. R. ARMSTRONG, D. E. MCCREADY, G. D. MAUPIN, G. W. COFFEY and C. A. COYLE, *J. Amer. Cer. Soc.* **80** (1997) 2109.
16. E. BERGSMARK, S. FURUSETH, O. DYRLIE, T. NORBY and P. KOFSTAD, in "Proceedings of the Second International Symposium on Solid Oxide Fuel Cells," edited by F. Grosz, P. Zegers, S. C. Singhal and O. Yamamoto, (Commission of European Communities, Luxembourg, 1991) p. 473.
17. L. A. CHICK, L. R. PEDERSON, G. D. MAUPIN, J. L. BATES, L. E. THOMAS and G. J. EXARHOS, *Mater. Lett.* **10** (1990) 6.
18. L. A. CHICK, G. D. MAUPIN, G. L. GRAFF, L. R. PEDERSON, D. E. MCCREADY and J. L. BATES, *Mater. Res. Soc. Symp. Proc.* **249** (1992) 159.
19. M. I. MENDELSOHN, *J. Amer. Ceram. Soc.* **52**(8) 443–446 (1969).
20. G. R. ANSTIS, P. CHANTIKUL, B. R. LAWN and D. B. MARSHALL, *ibid.* **64** (1981) 533.
21. W. F. BROWN and J. E. SRAWLEY, "Special Technical Publication 410" (American Society for Testing and Materials, Philadelphia, PA, 1966) pp. 13–14.
22. E. SCHREIBER, O. L. ANDERSON and N. SOGA, "Elastic Constants and Their Measurement" (Wiley, New York, 1973) p. 35.
23. W. F. BROWN and J. E. SRAWLEY, "Special Technical Publication 410" (American Society for Testing and Materials, Philadelphia, PA, 1966) pp. 82–122.
24. F. F. LANGE and M. M. HIRLINGER, *J. Amer. Cer. Soc.* **70** (1987) 827.
25. M. F. ASHBY and R. M. A. CENTAMORE, *Acta. Metall.* **16** (1968) 1081.
26. P. LEMAITRE and R. PILLER, *J. Mater. Sci. Lett.* **7** (1988) 772–774.
27. E. A. GEISS, R. L. SANDSTORM, W. J. GALLAGHER, A. GUPTA, S. L. SHINDE, R. F. COOK, E. J. M SULLIVAN, J. M. ROLDAN, A. P. SEGMULLER and J. ANGILELLO, *IBM J. Res. Develop.* **34**(6) (1990).
28. A. PETRIC, P. HUANG and AN. SKOWRON, in "Proc. of the 2nd European Solid Oxide Fuel Cell Forum," edited by B. Thorstensen (European SOFC Forum, Oslo, Norway, 1996) p. 751.
29. F. F. LANGE, *J. Mater. Sci.* **17** (1982) 240–246.
30. S. W. PAULIK, S. BASKARAN and T. R. ARMSTRONG, *ibid.* **33** (1998) 2397–2404.
31. K. KOBAYASHI, H. KUWAJIMA and T. MASAKI, *Solid State Ionics* **3/4** (1981) 489–493.
32. O. YAMAMOTO, Y. TAKEDA, N. IMANISHI, T. KAWAHARA, G. Q. SHEN, M. MORI and T. ABE, in "Proceedings of the Second International Symposium on Solid Oxide Fuel Cells," edited by F. Grosz, P. Zegers, S. C. Singhal and O. Yamamoto (Commission of European Communities, Luxembourg, 1991) p. 437.
33. Ceramics and Glasses, Engineered Materials Handbook, Vol. 4, edited by S. J. Schneider (ASM International, USA 1991) pp. 748–757.
34. J. S. NADEAU and J. I. DICKSON, *J. Amer. Cer. Soc.* **63** (1980) 517–523.
35. K. T. FABER and A. G. EVANS, *Acta Met.* **31** (1983) 565–576.
36. F. TIETZ, "Ninth International Conference on Modern Materials and Technologies" (CIMTEC '98), Florence, Italy, June 14–19, 1998.
37. P. R. SLATER, J. T. S. IRVINE, T. ISHIHARA and Y. TAKITA, in "Proceedings of the Third European Solid Oxide Fuel Cell Forum" (European Fuel Cell Forum, Oberrohrdorf, Switzerland, 1998) pp. 387–396.

Received 21 September 1998
and accepted 12 February 1999